Chemical Science

Accepted Manuscript

This article can be cited before page numbers have been issued, to do this please use: L. Zhang, F. Gao, Y. Wei, C. Zhong, B. Xia, L. Wen, Y. Long and Y. Ying, *Chem. Sci.*, 2026, DOI: 10.1039/D6SC03524H.

ROYAL SOCIETY OF CHEMISTRY

rsc.li/chemical-science

View Article Online
DOI: 10.1039/D6SC03524H

EDGE ARTICLE

Orthogonal Nanopores Cross-Validation for Multiplex Single-Molecule Profiling

Received 00th January 20xx,
Accepted 00th January 20xx

DOI: 10.1039/x0xx00000x

Lin-Lin Zhang,[a] Fan Gao,[a] Yi-He Wei,[a] Cheng-Bing Zhong,[a] Bingqing Xia,[b,c] Liuqing Wen,[c,d] Yi-Tao Long [a] and Yi-Lun Ying *[a,e]

Multiplex biomolecule profiling provides comprehensive molecular insights essential for precision health diagnosis. However, the difficulty arises from the fundamental diversity of biomolecules. Their sizes, charges, structures, and chemical compositions differ dramatically that achieving a simultaneous molecular profiling of multiple biomolecules, such as DNAs, RNAs, peptides, oligosaccharides, and metabolites remains inherently challenging. Herein, we present a Nanopore Multiplex Sensor (NMS) based on bioelectronic microchip that enables concurrent profiling of multiple biomolecules in a single experiment, which was previously unattainable. Further cross-validation using multiple types of orthogonal nanopores with complementary recognition abilities offers the simultaneous detection and relative quantitation of five major types of biomolecules relevant to non-small cell lung cancer. Our work establishes a robust and generalizable nanopore platform for rapid and parallel biomarker sensing, providing an important step toward addressing the vital challenge of deciphering molecular diversity through single-molecule multi-omics.

Introduction

Precision medicine and understanding of complex biological systems require systematic investigation across a diverse set of biomolecules.[1,2] Disease progression network is characterized by broad changes in biomolecular composition and abundance at the single-molecule level.[3,4] To capture such complexity, multiplex technologies have been developed to integrate different layers of biological information, as reliance on a single type of biomolecule often yields an incomplete or even misleading view of biological states.[5,6] Single-molecule multiplex biomolecule sensing reveals molecular heterogeneity and temporal molecular dynamics through direct and complementary analysis of individual biomolecules. Conventional multiplex techniques, such as mass spectrometry, sequencing, and fluorescence, can detect more than one biomolecular type,[7-9] yet still face several critical bottlenecks. (1) Difficulty in simultaneous single-molecule sensing of diverse biomolecules. Nucleic acids, proteins, glycans, and etc., differ in greatly physicochemical properties and detection efficiency, making it difficult to unify sample preparation, separation, and detection within a single analytical workflow. As a result, different biomolecular types are often measured separately, limiting comprehensive and simultaneous profiling. Morever, traditional techniques generally offer averaged informaton, obscuring molecular dynamics behaviors. (2) Reliance on complex labeling processes. The isotopic, chemical or fluorescent labeling is often required for accurate quantification and multiplexing. However, these labeling and probe-based strategies introduce additional cost and operational complexity, potentially increasing false-positive bias and perturbation of native biomolecular states. Moreover, multiplex capacity is often constrained by signal overlap, label compatibility, and the limited number of distinguishable labels, thereby restricting the analyzed number of molecules in a single process. (3) Lack of integration and efficiency. Existing platforms rely on discrete, labor-intensive workflows with limited parallel capacity, usually requiring hours to days from sample preparation to data analysis. These processes limit their suitability for rapid, high-throughput multiplex biomolecule profiling, falling short of the growing demand for timely and actionable insights in biological sensing instantly. Therefore, these limitations highlight the urgent needs for developing a generalized multiplex platform which is capable of diverse biomarkers sensing in a rapid, label-free, and scalable manner at the single-molecule level.

Nanopore is a label-free and easily integrated single-molecule electrochemical sensing technique capable of capturing specific and transient ionic current signatures of individual biomolecules with high sensitivity and resolution.[10,11] To date, biological nanopore offers high sensitivity and selectivity governed by its intrinsic physical and chemical properties of the sensing interface, such as pore size, geometry, and surface charge.[12-14] These characteristics make it desirable for diverse biomolecules sensing separately, including DNAs, RNAs, peptides, oligosaccharides, and small-molecule metabolites.[15-

[a] Molecular Sensing and Imaging Center, School of Chemistry, Nanjing University, Nanjing 210023 (P. R. China). E-mail: yilunying@nju.edu.cn
[b] School State Key Laboratory of Drug Research, Shanghai Institute of Materia Medica, Chinese Academy of Sciences, Shanghai 201203 (P. R. China).
[c] University of Chinese Academy of Sciences, Beijing 100049 (P. R. China).
[d] Carbohydrate-Based Drug Research Center, Shanghai Institute of Materia Medica, Chinese Academy of Sciences, Shanghai 201203 (P. R. China)
[e] Chemistry and Biomedicine Innovation Center, Nanjing University, Nanjing 210023 (P. R. China)

View Article Online
DOI: 10.1039/D4SC03524H

[20] Such advances establish nanopore as a promising solution for multiplex single-molecule sensing with temporal dynamics, positioning it as an emerging platform for multiplex analysis without relying on labeling or probe-based strategies. However, as each nanopore is typically suited to a specific range of molecular dimensions and properties, a single type of nanopore is hard to efficiently detect a broad range of biomolecules required for multiplex detection. This limitation highlights the need to integrate multiple types of orthogonal nanopores with complementary sensing capabilities for cross-validation, enabling reliable and comprehensive molecular recognition. Moreover, the limited integration and compatibility of current sensors further constrain their practical implementation. Dependence on external electrodes and discrete amplifiers increases device footprint and introduces electrical noise, while the large volume per channel raises sample consumption, together restricting system scalability, applicability and adding operational complexity.[21,22] Although several reported microchip platforms have well incoporated multi-channel recording capabilities,[23,24] they typically rely on a single type of nanopore for each biomolecule class, limiting their ability to perform genuine multiplex capability.

Herein, we address these challenges by developing a Nanopore Multiplex Sensor (NMS) for single-molecule multiple biomolecules sensing (Fig. 1). NMS integrates diverse orthogonal nanopores into a multi-chamber microchip with built-in film electrodes and ultra-low-current amplifier array, enabling label-free, high signal-to-noise ratio (SNR), high-throughput and high-sensitivity sensing. The parallel recording of ionic current captures distinct signals from each sample across multiple nanopore types, enabling the sensing of a wide range of biomolecules. Adopting machine learning algorithms and linear fitting models, this cross-validation approach enables robust qualitative and relatively quantitative analysis of multiple biomolecules spanning heterogeneous sizes, weights and charges, such as circulating tumor DNA (ctDNA) segments, microRNA (miRNA) segments, tumor-associated proteins fragments and their glycosylation, and small-molecule metabolites. Implementation of the parallel cross-validation strategy in NMS establishes an important step toward rapid multiplex sensing, paving the way for precision diagnosis and elucidation of molecular mechanism.

Results and discussion

Design of nanopore multiplex sensor

The bioelectronic microchip adopts a three-layer architecture according to our previous study[25] consisting, from bottom to up, of a smooth SiO_2 substrate with a low dielectric constant, patterned Ag/AgCl electrode arrays and Au wires, and a hydrophobic supporting layer for stable membrane array (Materials and Methods in Supplementary Information). Specially, to accommodate multiple types of nanopores on a single run, the low noise bioelectronic microchip features six spatially partitioned chambers, each functionalized with a specific nanopore type for simultaneous sensing of various biomolecules. Each chamber integrates four independent $Ag/AgCl_{trans}$ microelectrodes and one $Ag/AgCl_{cis}$ electrode that enhance experimental throughput and reproducibility (Fig. S1).

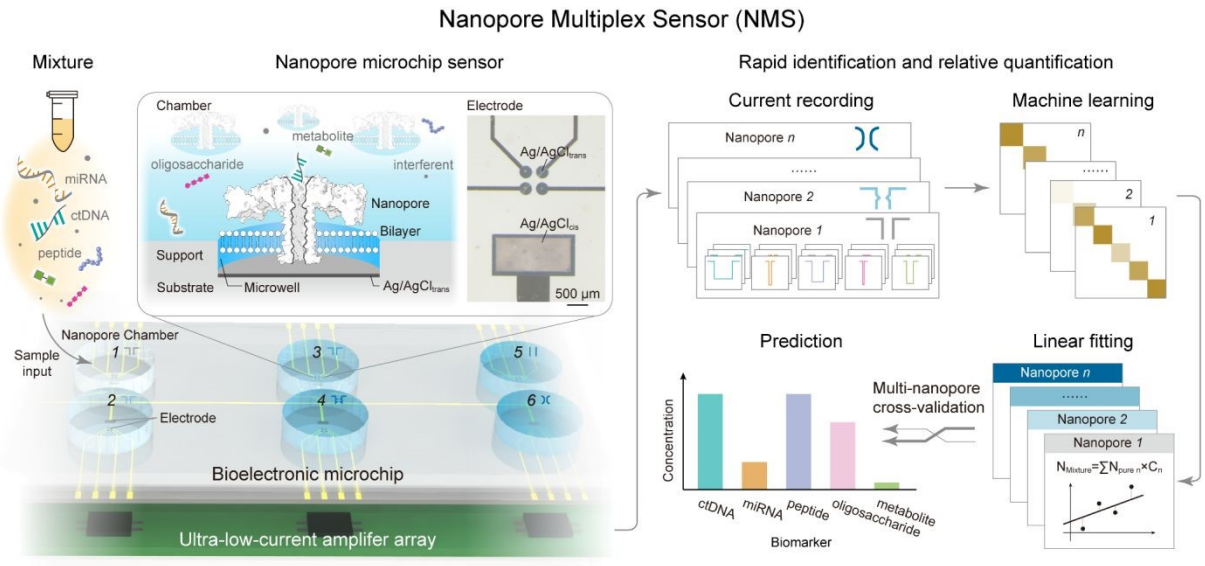

Fig. 1 Schematic illustration of the single-molecule nanopore multiplex sensor. The bioelectronic nanopore microchip features a three-layer design consisting of a substrate, electrode and bilayer-supporting layer, which is directly connected with an ultra-low-current amplifier array via Au wires patterned on the microchip for parallel measurements. Spatially separated sensing chambers integrate Ag/AgCl electrode-pair arrays and microwell arrays, with each chamber accommodating a distinct type of nanopore to enable simultaneous multiplex single-molecule sensing. Mixture samples, such as ctDNA segments, miRNA segments, peptides, oligosaccharides, and small-molecule metabolites, are introduced into a single microchip to generate parallel ionic current signals. These signals are processed through machine learning classification combined with multi-nanopore cross-validated linear fitting models, enabling rapid identification and relative quantification of multiplex biomolecule within minutes.

Integrated electrode pairs were prepared by electron beam evaporation (EBE) at the bottom of each chamber, eliminating the need for external hanging electrodes and thereby improving integration. Subsequently, an microwell array was patterned by photolithograph SU-8 coating serving as the supporting layer for bilayer formation (Fig. S2). $Ag/AgCl_{cis}$ as ground electrode was further electroplated via chronoamperometry on the EBE layer to increase thickness and robustness (Fig. S3). After Ag deposition and chlorination, the spacing between electrode and supporting layer decreased by ~3 μm, corresponding to the formation of Ag/AgCl layer (Fig. 2a). The open-circuit potential (OCP) remained stable during measurements, confirming the good stability and reusability of the integrated electrodes under our experimental conditions (Fig. 2b). Note that minor potential offsets could be corrected via software-based voltage compensation before single-channel recording. The microchip was directly connected with a homemade multi-channel ultra-low-current amplifier, where the shortened wiring effectively reduced noise, enabling simultaneous and independently controlled current recording. As shown in Fig. 2c, the integrated platform exhibited low baseline current noise, with a standard deviation (STD) of 0.5 ± 0.1 pA after nanopore insertion, substantially lower than that of conventional setups (~2.0 pA at 5 kHz low pass filter (LPF)).[26] This high SNR enables clearly identification of ionic current changes as low as 1.5 pA (with the threshold of three times the baseline STD). Benefiting from its compact chamber volume of 100-200 μL, the platform reduces sample consumption to the nanogram scale, further extending its applicability to low-volume and low-abundance biological samples. Therefore, this microchip configuration enables high-SNR, reliable and parallel multiplex biomolecules detection.

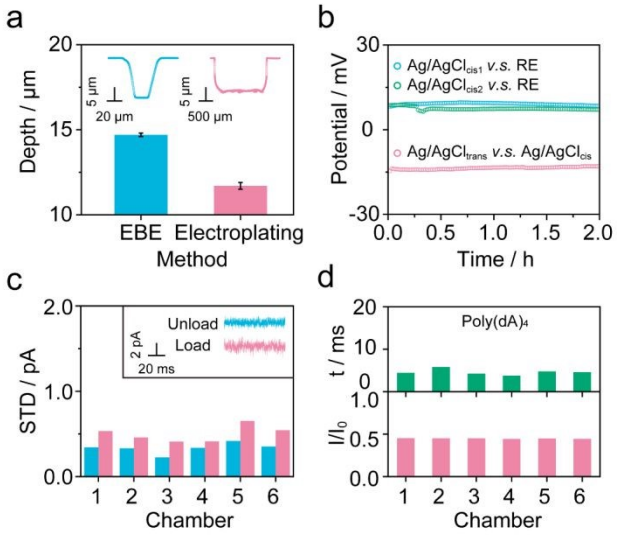

Fig. 2 Stability characterization of the nanopore multiplex sensor. (a) The depths between the supporting layer and the electrode layer. The inset scatter plots represent profilometer traces from a single measurement, showing the height profile from the SU-8 surface down to the $Ag/AgCl_{trans}$ (EBE) of 14.7 ± 0.1 μm or $Ag/AgCl_{cis}$ (Electroplating) of 11.7 ± 0.2 μm, and back to the SU-8 surface. The error bars were calculated from three independent measurements. (b) OCP of Ag/AgCl electrodes on a single microchip. Blue: OCP between the integrated $Ag/AgCl_{cis}$ electrode and a commercial Ag/AgCl electrode as a reference electrode (RE). Green: OCP measured after re-oxidation of the $Ag/AgCl_{cis}$ electrode following one round of nanopore experiment *v.s.* RE. Pink: OCP of the integrated $Ag/AgCl_{trans}$ microelectrode *v.s.* $Ag/AgCl_{cis}$ electrode in the one chamber. (c) The STD values of baseline current. One random channel in each chamber on the one microchip was selected for current noise testing. Blue: the noise of unloaded channels with only microchip connected to the amplifier array of 0.3 ± 0.1 pA. Pink: the noise level of open-pore current (I_0) with WT AeL loaded of 0.5 ± 0.1 pA at +100 mV. The inserted scatter plots showed typical baseline current under unload and nanopore inserted membrane conditions. (d) Statistical analysis of $Poly(dA)_4$ detection with WT AeL across six channels in six distinct chambers on the one microchip. Green: fitted distributions of duration time (t) of 4.6 ± 0.7 ms. Pink: fitted distributions of residual current depth (I/I_0) of 0.45 ± 0.01. Here, I represents the blockade residual current. The data were recorded with 100 kHz sampling rate and 5 kHz LPF.

To assess the performance of the platform, $Poly(dA)_4$ (5'-AAAA-3') was detected as a model analyte with the wild-type (WT) Aerolysin (AeL) nanopore across all chambers, owing to its well-established reproducibility and stability for single-molecule sensing.[26,27] The minor noise variations among different chambers may originate from instrumental and microchip manufacturing non-uniformity. Nevertheless, the recorded current blockades and event durations remained comparable across channels and microchips, agreeing with the single-channel platform results (Fig. 2d, Fig. S4-S6). Further, $Poly(dA)_4$ sensing with WT AeL in one chamber served as an internal reference for microchip calibration, facilitating robust normalization and accurate quantification.

Orthogonal nanopores for complementary detection

Since each type of nanopore is typically suited to a specific range of molecular dimensions and chemical properties, a single nanopore can hardly efficiently detect a broad type of biomolecules. Herein, we designed a series of orthogonal protein nanopores with complementary sensing capabilities. The engineered AeL and Outer membrane protein F (OmpF) nanopores were selected owing to their highly confined environment for high-sensitivity sensing of small biomolecules.[28] Specifically, the K238Q (KQ) AeL nanopore[29] with strong electrostatic interactions was employed for detecting charged single-stranded DNAs (ssDNAs) and short RNAs; the T232K/K238Q (TK/KQ) mutant AeL[30] with narrower pore diameter and strengthened interactions to improve the SNR for peptides and small-molecule metabolites; while the WT OmpF nanopore[31] with narrow constriction and stereoselectivity toward glycosidic bonds for oligosaccharides detection. All types of nanopore were produced in our laboratory with high stability (Fig. S7). Therefore, integrating these nanopores enables complementary molecular recognition and improves the multiplex sensing capability of the platform.

Using non-small cell lung cancer (NSCLC)-related biomolecules as a representative model,[32,33] we included the oligonucleotide from WT Epidermal Growth Factor Receptor (EGFR) and its mutant T790M ctDNA segments reflecting drug resistance;[34,35] miR-21 and miR-92a segments related to early diagnosis and oncogenicity;[36-38] peptide fragments of Programmed Cell Death Ligand 1 (PD-L1) and its phosphorylation at Tyr (p-PD-L1) [39-41],

View Article Online
DOI: 10.1039/D5SC07524H

as well as the N-linked glycosylation polylactosamine (DiLacNAc) from PD-L1 indicating immune regulation and evasion;[42-45] and Flavin Adenine Dinucleotide (FAD) representing metabolic dysfunction[46,47] (the sequence of each molecule was shown in Table S1). Simultaneous detection of EGFR, miR-21, PD-L1 and its glycosylation as well as FAD in body fluids enables complementary characterization of tumor progression, immune regulation, and metabolic dysfunction, highlighting the potential of multiplex nanopore sensing for comprehensive lung cancer profiling. Together, these biomolecules span genomic, transcriptomic, proteomic, glycomic, and metabolomic layers, providing an integrated view of tumor diagnosis and therapeutic response.

As shown in Fig. 3 and Fig. S8, each type of nanopore was evaluated through all these analytes separately, and assessed their sensing performance through capture frequency (*f*), *t*, and full width of half maximum (*FWHM*) of I/I_0. While the KQ AeL is responsive to oligonucleotides, miRNAs segments, peptides and small-molecule metabolites, it shows the highest discrimination ability for WT EGFR ctDNA and its T790M mutant segment own to narrower *FWHM* (Fig. S9). Due to the high capture rate and long duration time of the analyte, the TK/KQ AeL nanopore can effectively differentiate miR-21 and miR-92a segments, peptide fragments from PD-L1 with or without tyrosine phosphorylation, as well as small metabolic molecules such as FAD. WT OmpF reliably detects DiLacNAc as well as other oligosaccharides as

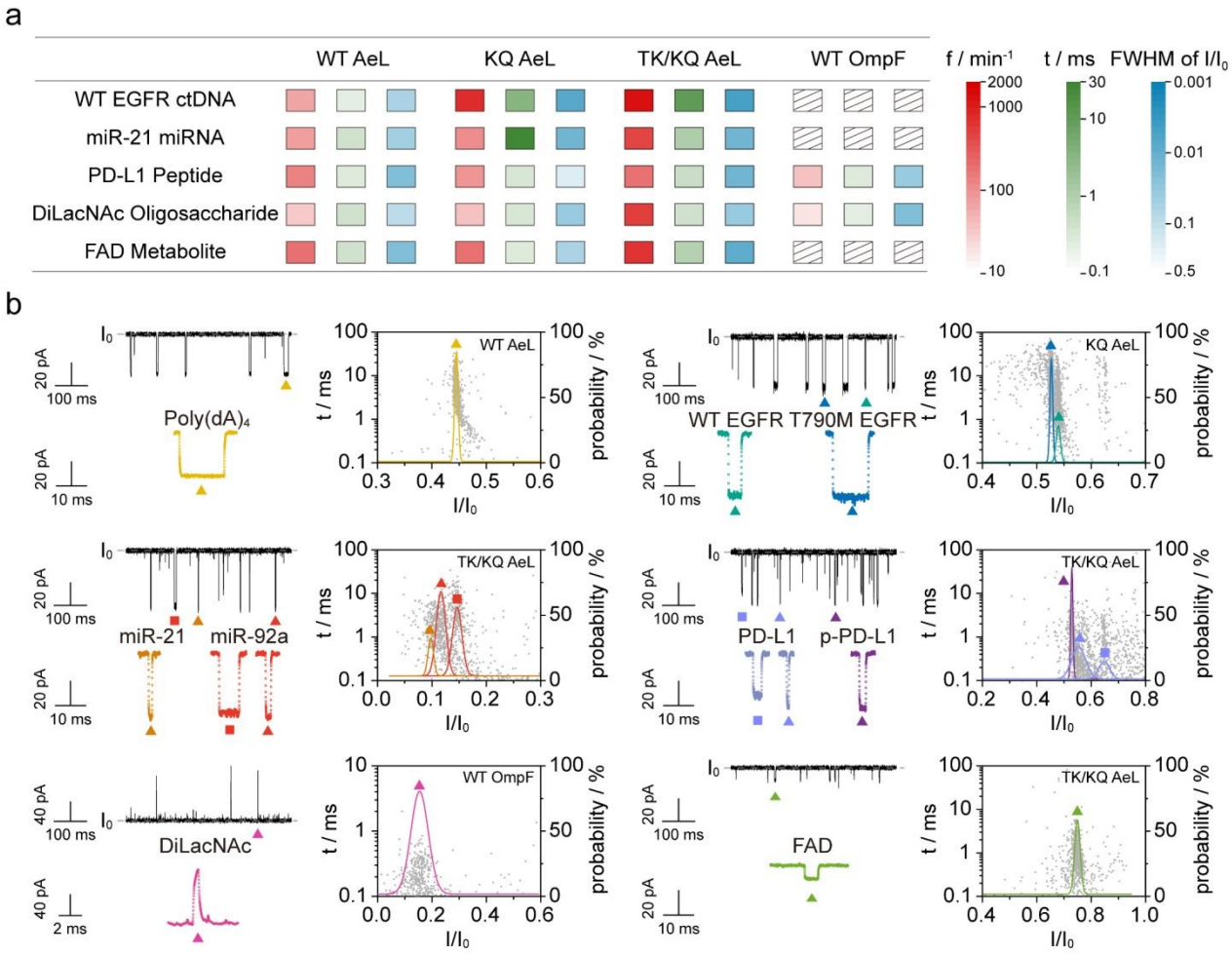

Fig. 3 Multiplex biomolecules detection with orthogonal nanopores. (a) Sensing characteristics including *f* (red), *t* (green) and *FWHM* of I/I_0 (blue) for the detection of five types of biomolecules with four nanopores, respectively. Diagonal lines indicate few signals produced preventing statistically analyzed. The darker colors indicate stronger sensing capability of a given nanopore towards a specific biomolecule. All color scales are presented on a logarithm scale to facilitate comparison. (b) The current trace, typical events, scatter plots of the I/I_0 versus *t*, and Gaussian fits of the histograms of I/I_0. From left to right and top to bottom: Detection of 2 μM $Poly(dA)_4$ with WT AeL at the applied voltage of +100 mV with 1000 events. Detection a mixture of 2 μM WT EGFR and 2 μM T790M EGFR segments with KQ AeL at +140 mV (2000 events) showed larger blockage current for T790M EGFR segments. Detection of a mixture of 5 μM miR-21 and 5 μM miR-92a segments using TK/KQ AeL at +100 mV (1000 events) showed two peaks from miR-92a exhibiting longer *t* and larger I/I_0 compared to miR-21. Detection a mixture of 2 μM PD-L1 peptide and 2 μM p-PD-L1 with TK/KQ AeL at +140 mV (2000 events) showed longer *t* for p-PD-L1 compared to PD-L1. Detection of 1 mM DiLacNAc with WT OmpF at -100 mV with 400 events. Detection of 2 μM FAD with TK/KQ AeL at +80 mV with 1000 event. All data were recorded in 1.0 M KCl, 10 mM Tris, pH 8.0, with a sampling rate of 100 kHz and a LPF of 5 kHz using the homemade multichannel microchip and instrument.

View Article Online
DOI: 10.1039/D5SC07524H

describe in the previous work,[31] likes human milk oligosaccharide (HMO)[48] motifs (Fig. S10), whereas other nanopores yield few events.

Multi-nanopore cross-validation for multiplex biomolecule sensing

Collectively, these current signatures from multiple nanopores under identical on-chip experimental conditions constitute a consistent, high-quality dataset suitable for comparative sensing while reducing measurement discrepancies arising from different sensing approaches. Taking advantage of these reliable measurements, we implemented a machine learning (ML) strategy[49,50] based on a Random Forest model for rigorous, high-throughput and automated profiling of current signals (Fig. 4a and Fig. S11). Since the events features of I/I_0 and t were highly reproducible, these two parameters were selected for model training and validation. In order to reduce interference, the Hierarchical Density-Based Spatial Clustering of Applications with Noise (HDBSCAN) algorithm was applied as a pre-clustering denoising processing. For each nanopore type, analytes with fewer events were excluded to prevent overfitting and ensure robustness. The cross-validation confusion matrixes and learning curves for the four nanopores were shown in Fig. S12-S13. Then, the ML models were used in mixture identification of WT EGFR, miR-21, PD-L1, DiLacNAc, and FAD using several nanopores.

However, using a single type of nanopore struggles to simultaneously identify all types of analytes due to their selectivity differences, which easily introduces false positives and false negatives in multiplex sensing. Herein, a multiple-nanopore-based linear fitting model enables cross-validated quantitation using concentration-dependent event counts from each nanopore. As demonstrated in previous works[10,49,51-53], the frequency of single-molecule translocation events shows a linear relationship with analyte concentration,

$$N=\alpha\times N^{[C]} \quad (1)$$

where N is the number of machine learning-predicted events for mixture sample, α is the fitted coefficient, and $N^{[C]}$ is the classified number for a pure sample at known concentration ($[C]$). Therefore, for each analyte (i), the predicted concentration C_i of each nanopore was directly calculated from the number of ML predicted events using:

$$C_i=\alpha\times[C_i] \quad (2)$$

where $\alpha = N/N^{[C]}$. Using this relationship, all analytes in each

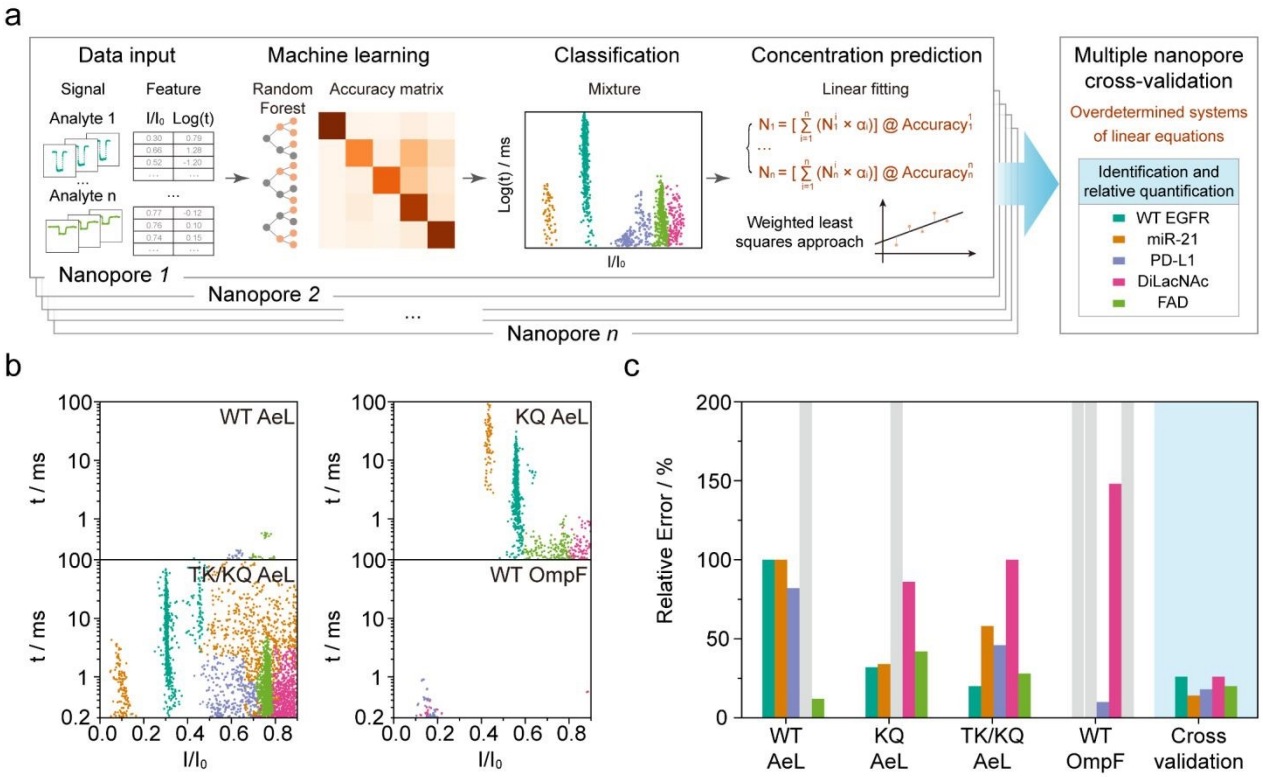

Fig. 4 Cross-validation using parallel orthogonal nanopores for multiplex biomolecules profiling in mixtures. (a) Schematic diagram of the NMS for relative quantitation using multiple nanopores for cross-validation. Machine learning with the linear fitting model enables identification and concentration prediction of each analyte. (b) Classification scatter plots predicted by ML models were obtained from a mixture sample containing 1 μM WT EGFR, 2.5 μM miR-21, 1 μM PD-L1, 0.5 mM DiLacNAc, and 1 μM FAD detection with WT AeL, KQ AeL, TK/KQ AeL at +100 mV, and WT OmpF at -100 mV in 3 min respectively. (c) Concentration prediction error for mixture containing 5 types of analytes: 1 μM EGFR, 2.5 μM miR-21, 1 μM PD-L1, 0.5 mM DiLacNAc and 1 μM FAD. Relative error is equal to the absolute value obtained by subtracting the true value from the predicted value, and then dividing by the true value. The Gray represents the incapability of nanopore sensing for this type of analyte. Blue bars highlight the lowest error achieved by the multi-nanopore cross-validation method for five types of biomolecules. All data were recorded with the sampling rate of 100 kHz and filtering at 5 kHz using homemade microchip and amplifier array.

View Article Online
DOI: 10.1039/D6SC03524H

nanopore yields independent linear equations (3),

$$N_i=\alpha_1\times N_i^{[C1]}+\ldots+\alpha_i\times N_i^{[Ci]}+\ldots+\alpha_n\times N_i^{[Cn]} \quad (3)$$

where N_i is the classified number of each analyte in the complex sample, α_i is the fitted concentration coefficient of each analyte, $N_i^{[Ci]}$ is the number of each pure analyte at known concentration ($[C_i]$) which was classified as analyte i, and n is the type of analyte in total. Equation (3) describes the multivariate linear equations formed by a single nanopore for all analytes sensing, with each equation corresponding to each analyte classified counts in mixture. By jointly solving these overdetermined equations across all nanopores, the concentrations of analytes in the mixture are predicted. To reduce prediction errors, we weighted each nanopore's data by its classification accuracy in ML model. Given that the statistical event frequency remains constant at a fixed analyte concentration, data collected over 3 min were analyzed using weighted least squares (WLS) fitting for reliable prediction (Table S2-S4). To validate this approach, we first applied it to simulated datasets mimicking complex samples. As shown in Fig. S14, the predicted concentrations closely matched the real values across mixtures with different concentration ratios, confirming the feasibility and reliability of the model. We then extended this method to experimental data, which also showed good agreement with the theoretical input. For example, in mixtures containing 2 or 3 analytes, the cross-validation model could well identify the components and predicted their concentrations (Fig. S15-S16, Table S5-S6). Although a single nanopore can in principle detect several molecule types, its differential sensing ability across analytes often leads to prediction deviations (Fig. S16). When 5 analytes were mixed together for validation, the multiple-nanopore cross-validation method consistently yielded lower relative errors (Fig. 4b-4c, Table S7). By integrating weighted linear fitting across four different types of nanopores, our method exploits the complementary strengths of each nanopore, thereby substantially improving the accuracy and robustness of molecular identification and quantification, and establishing a reliable stragety for multiplex biomolecule sensing.

To evaluate real-sample compatibility, the ML model was further applied to identify a mixture of WT EGFR, miR-21, PD-L1, DiLacNAc, and FAD in the presence of 1% fetal bovine serum (FBS), enabling evaluation of its stability within a complex and nonspecific molecular background. Each nanopore accurately recognized its preferred targets despite the complex background, demonstrating the potential of NMS for clinical samples sensing (Fig. S17-S19). However, at high analyte concentrations, nanopore becomes saturated by multiple molecule translocations[54,55], which decreases sensitivity to coexisting molecules (Fig. S20-S21). Conversely, low-abundance analytes may yield too few events submerged in background noise to enable reliable quantification.[56] To address these challenges, we defined the upper detection limit of concentration as the minimum resolvable event interval time of 10 ms (Table S8-S9). The lower detection limit was set at twice the background events frequency over a 3-minute window (Table S9). The prediction accuracy gradually improved with increasing numbers of integrated nanopores (Fig. S22), suggesting that further incorporation of more orthogonal nanopores could potentially provide additional improvements in prediction performance. To further increase throughput and experimental efficiency, we implemented a microchip-based automated system compatible with liquid handling automation, enabling standardized membrane assembly and parallelized workflows. As shown in Fig. S23, for validation, six chambers produced consistent and reproducible measurments. By integrating the quantitative model with the automated platform, NMS paves the way for efficient, reproducible and high-throughput multiplex single-molecule sensing.

Conclusions

Herein, we developed a nanopore multiplex sensor that integrates a series of orthogonal nanopores into a low noise bioelectronic microchip platform for multiplex biomolecules sensing. Through the combination of machine learning classification with multi-nanopore-driven linear fitting modeling, NMS achieves rapid identification and relative quantification of diverse analytes in mixture. This platform reduces the need for labor-intensive standard curve generation and cross-approach calibration with enhanced accuracy through multi-nanopore cross-vaidation. The NMS exhibits high integrity, stability, accuracy, and efficiency, enabling simultaneous, time-resolved multiplex biomolecule sensing from a single, low-volume sample. Such an integrated orthogonal nanopore platform would improve data comparability and measurement throughput by minimizing variability arising from separate measurements and batch-to-batch differences. Furthermore, the capability for concurrent analysis of biomarkers involved in molecular cross-talk might facilitate the capture of temporally correlated molecular variations, providing more comprehensive insights into disease progression, molecular regulation, and therapeutic response.

The employed orthogonal nanopores of AeL and OmpF own inherent benefits in detecting short biomolecules due to narrow nanopore size, offering high sensitivity for single-nucleotide discrimination, post-translational modification detection, and small molecule sensing. Extending NMS's applicability to larger targets such as full-length DNA, proteins, and glycans will require enzymatic digestion or the adoption of larger nanopores such as ClyA, FhuA. Detection of low-abundance biomarkers in real samples will benefit from integration with upstream enrichment and separation strategies directly on-chip and nanopore-integrated. While validated results support system compatibility, further engineering and intelligent feedback control is still needed to enhance throughput, enable independent modular control, and facilitate integration with clinical sample processing pipelines. Further improvements in prediction accuracy could be achieved through advanced machine learning models with expanded multidimensional signal feature extraction, and optimized concentration prediction algorithms. By integrating more orthogonal nanopores with complementary sensing characteristics, NMS demonstrates the potential as a scalable framework not only for

DNA/RNA/peptide sequencing and single-omics analysis, but also for the concurrent sensing of diverse biomolecular types. Continued optimization in orthogonal nanopore engineering, microchip packaging, integrated circuits, and intelligent data analysis algorithms will further enhance NMS as an important complementary technology for multiplex biomarker sensing, potentially contributing to the development of next-generation precision molecular diagnosis and comprehensive single-molecule multi-omics analysis.

Author contributions

Y.-L. Y. and Y.-T. L. conceived the original idea of the research and supervised the project. L.-L. Z. designed the platform. L.-L. Z. and Y.-H. W. conducted the experiments. L.-L. Z. and F. G. performed machine learning and discission-making algorithm construction. C.-B. Z. design the multi-channel ultra-low-noise amplifier circuit. L.-L. Z. processed the data and wrote the manuscript. L. W synthesized oligosaccharides. All authors discussed the results and commented on the manuscript.

Conflicts of interest

There are no conflicts to declare.

Data availability

The data supporting this article have been included as part of the supplementary information (SI). Supplementary Information: materials, methods, and additional measurements.

Acknowledgements

The authors thank Dr. Meng-Yin Li, Jun-Ge Li, and Yan Gao from Nanjing University for aerolysin protein production and helpful discussion. This work was financially supported by National Key Research and Development Program of China (2022YFA1304604), National Natural Science Foundation of China (22334006, 22474055 and 22027806), Scientific Instrument Developing Project of the Chinese Academy of Sciences (PTYQ2024YZ0008), Jiangsu Province "Double First-Class" Initiative Grant (0205-1480601101) and the Fundamental Research Funds for the Central Universities (020514380356).

References

1 J. Wen, *Nat. Biomed. Eng.*, 2025, **9**, 1386-1389.
2 L. C. Kida and C. A. Lareau, *Nat. Methods*, 2025, **22**, 1135-1136.
3 M.-Y. Li, J. Jiang, J.-G. Li, H. Niu, Y.-L. Ying, R. Tian and Y.-T. Long, *Nat. Methods*, 2024, **22**, 241-253.
4 J. Tu, C. D. Flynn, J. Yeom, Z. Wu, S. O. Kelley and W. Gao, *Nat Nanotechnol.*, 2025, **20**, 1388-1404.
5 A. Baysoy, Z. Bai, R. Satija and R. Fan, *Nat. Rev. Mol. Cell Biol.*, 2023, **24**, 695-713.
6 J. Yin, Y. Zheng, Z. Huang, W. Zhou, Y. Yuan, P. Cai, Y. Bai, S. Yang, Y. Gao, S. Duan, Y. Wang, Z. Xu, W. Zhang, X. Zhang, Y. Wei, Y. Huang, Y. Liu, W. Wang, T. Yang, Z. Zhang, X. Chen, X. Zhang, J. Lv, F. Li, Y. Zhang, G. Zeng, X. Wang, W. Ma, G. Hou, S. Hao, C. Liu, Y. Lai, P. Liu, B. Wang, Y. Li, W. Zhang, P. Gao, J. Xie, M. A. Esteban, Y. Gu, X. Liu, J. Ji, T. Qi, B. Liu, H. Wang, Y. Zhao, X. Yang, X. Wang, R. Chen, J. Yang, Y. Yin, J. Wang, Y. Cao, X. Xu, L. Liu, X. Jin and C. Liu, *Science*, 2026, **391**, eadt3130.
7 Y. Zheng, Y. Liu, J. Yang, L. Dong, R. Zhang, S. Tian, Y. Yu, L. Ren, W. Hou, F. Zhu, Y. Mai, J. Han, L. Zhang, H. Jiang, L. Lin, J. Lou, R. Li, J. Lin, H. Liu, Z. Kong, D. Wang, F. Dai, D. Bao, Z. Cao, Q. Chen, Q. Chen, X. Chen, Y. Gao, H. Jiang, B. Li, B. Li, J. Li, R. Liu, T. Qing, E. Shang, J. Shang, S. Sun, H. Wang, X. Wang, N. Zhang, P. Zhang, R. Zhang, S. Zhu, A. Scherer, J. Wang, J. Wang, Y. Huo, G. Liu, C. Cao, L. Shao, J. Xu, H. Hong, W. Xiao, X. Liang, D. Lu, L. Jin, W. Tong, C. Ding, J. Li, X. Fang and L. Shi, *Nat. Biotechnol.*, 2024, **42**, 1133-1149.
8 X. Wang, H. Huang, S. Jiang, J. Kang, D. Li, K. Wang, S. Xie, C. Tong, C. Liu, G. Hu, H. Li, C. Li, L. Yang, Y. Ding, S.-T. Li, F. Wang, J. U. Lohmann, Z. Liang and X. Gu, *Nature*, 2025, **644**, 722-730.
9 T. Vu, A. Vallmitjana, J. Gu, K. La, Q. Xu, J. Flores, J. Zimak, J. Shiu, L. Hosohama, J. Wu, C. Douglas, M. L. Waterman, A. Ganesan, P. N. Hedde, E. Gratton and W. Zhao, *Nat. Commun.*, 2022, **13**, 169.
10 H. Bayley and P. S. Cremer, *Nature*, 2001, **413**, 226-230.
11 A. Dorey and S. Howorka, *Nat. Chem.,* 2024, **16**, 314-334.
12 Y.-L. Ying, Z.-L. Hu, S. Zhang, Y. Qing, A. Fragasso, G. Maglia, A. Meller, H. Bayley, C. Dekker and Y.-T. Long, *Nat. Nanotechnol.*, 2022, **17**, 1136-1146.
13 S. Pal, A. Naik, A. Rao, B. Chakraborty and M. M. Varma, *ACS Appl. Nano Mater.*, 2022, **5**, 8804-8810.
14 L. Ratinho, N. Meyer, S. Greive, B. Cressiot and J. Pelta, *Nat. Commun.*, 2025, **16**, 3211.
15 M. Zhang, C. Tang, Z. Wang, S. Chen, D. Zhang, K. Li, K. Sun, C. Zhao, Y. Wang, M. Xu, L. Dai, G. Lu, H. Shi, H. Ren, L. Chen and J. Geng, *Nat. Methods*, 2024, **21**, 609-618.
16 X. Wei, A. Choudhary, L. Y. Wang, L. Yang, M. J. Uline, M. Tagliazucchi, Q. Wang, D. Bedrov and C. Liu, *Sci. Adv.*, 2024, **10**, eadp8134.
17 Y. Yi, P. Song, Z. Li, J. Ju, G. Sun, Q. Ren, K. Zhou, L. Liu and H.-C. Wu, *Nat. Nanotechnol.*, 2025, **20**, 1079-1086.
18 G. Yao, B. Xia, F. Wei, J. Wang, Y. Yang, S. Ma, W. Ke, T. Li, X. Cheng, L. Wen, Y.-T. Long and Z. Gao, *J. Am. Chem. Soc.*, 2025, **147**, 1721-1731.
19 Q. Liu, Y. Ouyang, Y. Wang, S. Zhou, Y. Zhan and L. Wang, *Adv. Healthcare Mater.*, 2025, **14**, 2405058.
20 X. Zhang, X. Wang, Y. Zhang, D. Liu, X. Wei, Y. Shao, Z. Li and G. Huang, *Angew. Chem. Int. Ed.*, 2026, DOI: 10.1002/anie.202523298.
21 A. J. W. Hartel, S. Shekar, P. Ong, I. Schroeder, G. Thiel and K. L. Shepard, *Anal. Chim. Acta*, 2019, **1061**, 13-27.
22 A. Fragasso, S. Schmid and C. Dekker, *ACS Nano*, 2020, **14**, 1338-1349.
23 G. Baaken, M. Sondermann, C. Schlemmer, J. Ruhe and J. C. Behrends, *Lab Chip*, 2008, **8**, 938-944.
24 T. Tonooka, T. Osaki, K. Sato, R. Kawano and S. Takeuchi, *Sens. Actuators B Chem.*, 2021, **334**, 129643.
25 L.-L. Zhang, C.-B. Zhong, T.-J. Huang, L.-M. Zhang, F. Yan and Y.-L. Ying, *Chem. Sci.*, 2024, **15**, 8355-8362.
26 L.-L. Zhang, C.-B. Zhong, J.-G. Li, H.-Y. Niu, Y.-L. Ying and Y.-T. Long, *J. Electroanal. Chem.*, 2022, **915**, 116266.
27 Z.-L. Hu, Y.-L. Ying, M.-Z. Huo, X.-F. Kong, X.-D. Yu, J.-R. Zhang and Y.-T. Long, *J. Chem. Educ.*, 2020, **97**, 4345-4354.
28 L. Iesu, M. Sai, V. Torbeev, B. Kieffer, J. Pelta and B. Cressiot, *Chem. Sci.*, 2025, **16**, 9730-9738.
29 J. Wang, S.-C. Liu, Z.-L. Hu, Y.-L. Ying and Y.-T. Long, *J. Am. Chem. Soc.*, 2025, **147**, 1781-1791.
30 Y.-H. Fu, X. Li, L. Ma, Y.-J. Wan, L.-M. Zhang, Y.-L. Ying and Y.-T. Long, *J. Phys. Chem. C*, 2024, **128**, 1110-1115.
31 F. Gao, J. H. Wang, H. Ma, B. Xia, L. Wen, Y. T. Long and Y. L. Ying, *Angew. Chem. Int. Ed.*, 2025, **64**, e202422118.

32 M. Boeri, C. Verri, D. Conte, L. Roz, P. Modena, F. Facchinetti, E. Calabrò, C. M. Croce, U. Pastorino and G. Sozzi, *Proc. Natl. Acad. Sci. U.S.A.*, 2011, **108**, 3713-3718.

33 K.-Z. Chen, F. Lou, F. Yang, J.-B. Zhang, H. Ye, W. Chen, T. Guan, M.-Y. Zhao, X.-X. Su, R. Shi, L. Jones, X. F. Huang, S.-Y. Chen and J. Wang, *Sci. Rep.*, 2016, **6**, 31985.

34 A. Leal, N. C. T. van Grieken, D. N. Palsgrove, J. Phallen, J. E. Medina, C. Hruban, M. A. M. Broeckaert, V. Anagnostou, V. Adleff, D. C. Bruhm, J. V. Canzoniero, J. Fiksel, M. Nordsmark, F. A. R. M. Warmerdam, H. M. W. Verheul, D. J. van Spronsen, L. V. Beerepoot, M. M. Geenen, J. E. A. Portielje, E. P. M. Jansen, J. van Sandick, E. Meershoek-Klein Kranenbarg, H. W. M. van Laarhoven, D. L. van der Peet, C. J. H. van de Velde, M. Verheij, R. Fijneman, R. B. Scharpf, G. A. Meijer, A. Cats and V. E. Velculescu, *Nat. Commun.*, 2020, **11**, 525.

35 J. Lei, Y. Huang, W. Zhong, D. Xiao and C. Zhou, *Anal. Chem.*, 2020, **92**, 8867-8873.

36 Y. Chen, F. Yang, L. Zubovic, T. Pavelitz, W. Yang, K. Godin, M. Walker, S. Zheng, P. Macchi and G. Varani, *Nat. Chem. Biol.*, 2016, **12**, 717-723.

37 C. Lu, Z. Shan, J. Hong and L. Yang, *Int. J. Oncol.*, 2017, **51**, 235-244.

38 R. Tavallaie, J. McCarroll, M. Le Grand, N. Ariotti, W. Schuhmann, E. Bakker, R. D. Tilley, D. B. Hibbert, M. Kavallaris and J. J. Gooding, *Nat. Nanotechnol.*, 2018, **13**, 1066-1071.

39 Q. Zhang, R. Salzler, A. Dore, J. Yang, D. Ma, W. C. Olson and Y. Liu, *J. Proteome Res.*, 2018, **17**, 3932-3940.

40 L.-C. Chan, C.-W. Li, W. Xia, J.-M. Hsu, H.-H. Lee, J.-H. Cha, H.-L. Wang, W.-H. Yang, E.-Y. Yen, W.-C. Chang, Z. Zha, S.-O. Lim, Y.-J. Lai, C. Liu, J. Liu, Q. Dong, Y. Yang, L. Sun, Y. Wei, L. Nie, J. L. Hsu, H. Li, Q. Ye, M. M. Hassan, H. M. Amin, A. O. Kaseb, X. Lin, S.-C. Wang and M.-C. Hung, *J. Clin. Invest.*, 2019, **129**, 3324-3338.

41 X. Wang, X. Yang, C. Zhang, Y. Wang, T. Cheng, L. Duan, Z. Tong, S. Tan, H. Zhang, P. E. Saw, Y. Gu, J. Wang, Y. Zhang, L. Shang, Y. Liu, S. Jiang, B. Yan, R. Li, Y. Yang, J. Yu, Y. Chen, G. F. Gao, Q. Ye and S. Gao, *Proc. Natl. Acad. Sci. U.S.A.*, 2020, **117**, 6640-6650.

42 M. Miyake, N. Kohno, E. D. Nudelman and S.-i. Hakomori, *Cancer Res.*, 1989, **49**, 5689-5695.

43 H.-H. Lee, Y.-N. Wang, W. Xia, C.-H. Chen, K.-M. Rau, L. Ye, Y. Wei, C.-K. Chou, S.-C. Wang, M. Yan, C.-Y. Tu, T.-C. Hsia, S.-F. Chiang, K. S. C. Chao, I. I. Wistuba, J. L. Hsu, G. N. Hortobagyi and M.-C. Hung, *Cancer Cell*, 2019, **36**, 168-178.

44 J. Benicky, M. Sanda, Z. Brnakova Kennedy, O. C. Grant, R. J. Woods, A. Zwart and R. Goldman, *J. Proteome Res.*, 2021, **20**, 485-497.

45 Z. Duan, R. Shi, B. Gao and J. Cai, *J. Transl. Med.*, 2024, **22**, 705.

46 M.-Y. Li, Y.-Q. Wang, Y.-L. Ying and Y.-T. Long, *Chem. Sci.*, 2019, **10**, 10400-10404.

47 K. Awasthi, F. L. Chang, P. Y. Hsieh, H. Y. Hsu and N. Ohta, *J. Biophotonics.*, 2020, **13**, e201960210.

48 Y. Zhu, G. Luo, L. Wan, J. Meng, S. Y. Lee and W. Mu, *Crit. Rev. Biotechnol.*, 2021, **42**, 578-596.

49 M. Li, J. Wang, C. Zhang, X. Zhao, Y. Xiong, Y. Cao, D. Wang, X. Li, X. Liang and G. Qing, *ACS Nano*, 2024, **18**, 25155-25169.

50 R. Akita, A. Lysenko, K. A. Boroevich, T. Yokota, D. Kawai, R. Iizuka, T. Tsunoda and S. Uemura, *Chem. Sci.*, 2025, **16**, 18607-18615.

51 P. Waduge, R. Hu, P. Bandarkar, H. Yamazaki, B. Cressiot, Q. Zhao, P. C. Whitford and M. Wanunu, *ACS Nano*, 2017, **11**, 5706-5716.

52 N. S. Galenkamp, M. Soskine, J. Hermans, C. Wloka and G. Maglia, *Nat. Commun.*, 2018, **9**, 4085.

53 J. Jiang, M.-Y. Li, X.-Y. Wu, Y.-L. Ying, H.-X. Han and Y.-T. Long, *Nat. Chem.*, 2023, **15**, 578-586.

54 C. Plesa, D. Verschueren, S. Pud, J. van der Torre, J. W. Ruitenberg, M. J. Witteveen, M. P. Jonsson, A. Y. Grosberg, Y. Rabin and C. Dekker, *Nat. Nanotechnol.*, 2016, **11**, 1093-1097.

55 R. A. Lazenby, F. C. Macazo, R. F. Wormsbecher and R. J. White, *Anal. Chem.*, 2018, **90**, 903-911.

56 K. Chuah, Y. Wu, S. R. C. Vivekchand, K. Gaus, P. J. Reece, A. P. Micolich and J. J. Gooding, *Nat. Commun.*, 2019, **10**, 2109.

View Article Online DOI: 10.1039/D5SC03541H

View Article Online
DOI: 10.1039/D6SC03524H

Data Availability Statement

The data supporting this article have been included as part of the Supplementary Information (SI). Supplementary Information: materials, methods, and additional measurements.